Three-phase Reduced-sensor Modular Multilevel Converter with Distributed MPPT for PV Integration Based on Extended Kalman Filter

Marzio Barresi, *Member*, *IEEE*, Davide del Giudice, *Member*, *IEEE*, Davide de Simone, *Member*, *IEEE*, and Samuele Grillo, *Senior Member*, *IEEE*

***Abstract*—Modular multilevel converters (MMCs) have emerged as a promising solution for integrating renewables. In case of photovoltaic (PV) systems, PV arrays can be integrated at the submodule (SM) level, and the distributed maximum power point tracking (DMPPT) can be achieved through AC and DC circulating current control and perturb and observe (P&O) methods. However, this implementation is hindered by the need for numerous measurements, since the voltage and current of all PV arrays in each SM must be known. To address this issue, we propose a three-phase reduced-sensor MMC with distributed MPPT for PV integration based on an extended Kalman filter (EKF). For each MMC arm, the EKF estimates the voltage and irradiance of each SM by exploiting their gate signals and duty cycles as well as the arm current and voltage. This solution is compatible with uniform and non-uniform irradiance conditions both under the steady-state and transient conditions and uses significantly fewer sensors than other strategies employed in similar-purpose MMCs, while achieving comparable efficiency. Moreover, by exploiting the PV array characteristics, it allows performing DMPPT more directly, without using P&O methods. These features are confirmed by simulations of an MMC-based PV system with 12 SMs per arm.**

***Index Terms*—Modular multilevel converter (MMC), photovoltaic (PV), extended Kalman filter (EKF), maximum power point tracking (MPPT).**

I. INTRODUCTION

PHOTOVOLTAIC (PV) system is a key technology for the sustainable transition towards renewable-based grids. PV cells are the basic building block of such system: their series/parallel connection composes a module; moreover, the series connection of modules leads to a string that, if connected in parallel with others, forms a PV array. The maximum power point tracking (MPPT) algorithms are commonly employed to extract the maximum available power from PV systems [1]-[3]. However, their effectiveness is challenging for large PV systems under partial shading conditions when the irradiance on each PV module differs, as the MPPT algorithms tend to optimize the power extraction for the group of modules rather than for individual ones. In this case, the most common and simplest solutions do not allow each PV module to work at its maximum power point (MPP), which is inefficient and leads to sub-optimal operation [4]-[6]. Indeed, these solutions rely on a centralized approach where the converter interface is based on: ① a single-stage topology, where the entire PV system is interfaced through a single AC/DC converter equipped with MPPT [3], or ② a two-stage topology with an additional DC/DC converter between the main AC/DC converter and PV system, which regulates the DC-side voltage of main converter and performs the MPPT [7].

To improve the power generation of PV system, the distributed MPPT (DMPPT) algorithms can be used for individual PV arrays. To do so, each PV array must be connected through a dedicated power conversion stage, allowing the separate control of power flow [8]-[13]. Among the solutions proposed to implement DMPPT algorithms [14]-[19], integrating PV arrays at the submodule (SM) level of a modular multilevel converter (MMC) ranks among the most efficient and versatile ones [20]-[23].

MMCs deploy a cascaded connection of identical SMs, which uses relatively low-voltage semiconductors to implement high-voltage conversion systems with low-harmonic content of output current and many output voltage levels [24], [25]. Based on the SM structure and arrangement, multiple MMC families can be defined [26], each of which is suitable for different applications [27]-[29].

In the case of PV integration, PV arrays can be integrated at the DC side of MMCs or directly at the SM level. The latter solution is promising in the context of DMPPT implementation: as proven in [30] for a single-phase MMC, PV arrays can operate at their MPPs even under partial shading conditions. This is achieved without the need to connect each PV array to a dedicated DC/DC converter (which leads to additional costs), but rather by generating a suitable set of

---

Manuscript received: October 24, 2024; revised: January 29, 2025; accepted: June 17, 2025. Date of CrossCheck: June 17, 2025. Date of online publication: August 12, 2025.

This work was supported in part by the EU fund Next Generation EU, Missione 4, Componente 2, Investimento 1.3 CUP D43C22003090001, PE0000021 PNRR NEST Spoke 6 and in part by the EU fund Next Generation EU, Missione 4, Componente 1, CUP D53D23001650006, MUR PRIN project 2022ZJPPSN SCooPS.

M. Barresi, D. del Giudice (corresponding author), D. de Simone, and S. Grillo are with the Department of Electronics, Information, and Bioengineering (DEIB) at Polytechnic University of Milan, Milan, Italy (e-mail: marzio.barresi@polimi.it; davide.delgiudice@polimi.it; davide.desimone@polimi.it; samuele.grillo@polimi.it)

DOI: 10.35833/MPCE.2024.001154

circulating currents flowing through the MMC arms with the converter control scheme. If a three-phase MMC is used for PV integration, the efficiency can be further improved by connecting the DC side of MMC to a capacitor, which enables the injection of zero-sequence circulating current components [23]. Table I compares the converters for PV integration in different studies.

TABLE I
COMPARISON AMONG CONVERTERS FOR PV INTEGRATION

Ref.	Scheme of PV integration with different converters	Feature
[3]	PV plant is integrated through a single-stage three-phase inverter	√ Low component count √ Low computational burden √ Reduced number of sensors × Whole-stack MPPT, i.e., non-distributed MPPT
[7]	PV plant is interfaced with a dual-stage conversion system using a DC/DC partial power converter and an inverter	√ Low computational burden √ Single set of sensors for each PV array √ Higher control flexibility than [3] × Whole-stack MPPT, i.e., non-distributed MPPT
[8]	PV plant is divided into PV arrays, each of which is interfaced through a dedicated DC/DC power conversion stage	√ Higher control flexibility than [3] √ DMPPT capability √ Low computational burden × Strict requirement for independent sensor set per array × More complex control than [3]
[11]	PV plant is divided into PV strings connected in series, each of which integrates a parallel partial power converter	√ Higher control flexibility than [3] √ DMPPT capability √ Low computational burden √ More efficient than [8] with partial power converters × Strict requirement for independent sensor set per array × More complex control than [8]
[23]	PV plant is divided into PV arrays, each of which is integrated into SMs of MMC	√ Intrinsic DMPPT capabilities √ Dual-stage power conversion system elimination √ Multilevel output waveforms, i.e., low filtering requirements √ Fault-tolerant capability with modular structure × Complex control algorithm × Single set of measurements for each SM × Complex control hardware with many analog-to-digital converters
This paper	PV plant is divided into PV arrays, each of which is integrated into SMs of MMC. SM voltages and irradiances are estimated by an extended Kalman filter (EKF)	√ Intrinsic DMPPT capabilities √ No requirement for dual-stage power conversion system √ Multilevel output waveforms, i.e., low filtering requirements √ Fault-tolerant capability with modular structure √ Reduced set of measurements with EKF × Complex control algorithm

Note: √ and × represent the advantages and disadvantages, respectively.

Albeit more efficient and cost-effective than other solutions, the converter topologies enabling a distributed control suffer from a practical issue. Indeed, the DMPPT algorithms require the voltage and current measurements of each PV array as inputs: if the PV plant is integrated through MMC, which can include even tens of PV arrays in each arm, a large number of sensors are needed. This drawback is common for MMC-based applications, even if not meant for PV integration. For example, MMCs used in high-voltage DC (HVDC) systems, which rely on hundreds of SMs based on half-/full-bridge cells and a floating capacitor, require knowing the capacitor voltage of each SM to perform capacitor voltage balancing. To address the subsequent need for numerous measurements, the control strategies in Table II for sensor reduction in MMCs (with half-bridge SMs) are proposed.

In [31], a control strategy for MMCs that equalizes SM capacitor voltages is presented. Although effective, this strategy does not estimate individual capacitor voltages, which are needed in MMC-based PV systems to control SM voltages separately and implement DMPPT. In [32], an SM voltage balancing control is proposed, which relies neither on arm current sensors nor sorting techniques. However, this strategy still requires measuring all SM voltages. In [33], a sampling algorithm estimates SM voltages through arm voltage and current measurements. While this algorithm effectively reduces the number of sensors, it assumes that SMs are equipped with capacitors. Hence, it is not directly applicable to SMs with PV arrays.

Similarly, [34] and [35] introduce estimators (e.g., based on EKF and Lyapunov) that reduce the number of voltage sensors. However, like [33], these strategies are based on the assumption that the SMs contain exclusively capacitors, making them unsuitable for implementing DMPPT in SMs including PV. EKFs are also used in PV-related applications to estimate the irradiance and perform MPPT more easily than one would do with perturb and observe (P&O) methods [36], [37]. However, the irradiance is estimated by knowing the voltage and current of PV array. This requirement translates into the need for a high number of measurements in MMC, where PV arrays are integrated at the SM level—such as the ones we consider in this work.

TABLE II
COMPARISON AMONG CONTROL STRATEGIES FOR SENSOR REDUCTION IN MMCS

Ref.	Control strategy	Brief description	Feature of applicability to MMC-based PV systems [23]
[31]	Hierarchical permutation cyclic coding strategy	A gate signal control strategy that ensures SM capacitor voltage balancing is adopted without needing to measure/estimate SM voltages	× Do not measure/estimate SM voltages × Do not control each SM voltage separately, i.e., non-distributed MPPT × Assume all SMs have similar working points, which is not true for SMs integrating PV arrays
[32]	Currentless SM voltage balancing control for MMCs	All the SM voltages are measured. Instead of a sorting algorithm, a proportional-integral (PI) controller is used to balance the SMs, which does not rely on arm current measurements	√ Do not require external HVDC source to operate converter × Exploit external HVDC bus to balance SM voltages × Involve complex control × Measure all SM voltages, requiring many analog-to-digital converters
[33]	Improved SM capacitor voltage measurement algorithm for MMCs	SM voltages are estimated through arm voltage and current measurements with a sampling algorithm	√ Require only one voltage sensor per arm regardless of SM number × Rely on model of SM equipped with a capacitor for voltage estimation
[34]	EKF for full-state estimation and sensor reduction in MMCs	An EKF is used to estimate SM voltages through arm voltage and current measurements	√ Require only one voltage sensor per arm regardless of SM number × Rely on SM equipped with a capacitor for voltage estimation
[35]	Lyapunov-based observer for double-star chopper-cell (DSCC) converters	A Lyapunov-based observer is used for estimation of SM voltages	√ Require neither current nor voltage sensors regardless of SM number × Rely on SM equipped with a capacitor for voltage estimation
[36]	Voltage reconstruction strategy	An algorithm that samples SM voltages by adequately triggering and processing the measurement of just one voltage sensor per arm is used	√ Require only one voltage sensor per arm regardless of SM number × Require specific hardware to use multi-sampling technique × Suffer from unreliable sampled points

Finally, [36] proposes a sampling and processing algorithm capable of estimating all SM voltages of the converter using only one voltage sensor per arm. This control strategy is based on a multi-sampling technique that ① measures the arm voltages at a frequency that is $2N$ times higher than the switching frequency and ② eliminates unreliable data samples. Other than posing significant challenges in applications with multiple SMs (particularly in terms of hardware demands and peripherals, that is, analog-to-digital converters), this strategy is based on the assumption that SM integrates only a capacitor, whose voltage cannot exceed a predefined threshold between subsequent voltage acquisitions. However, this assumption does not necessarily hold for SM integrating PV sources under partial shading conditions, where rapid voltage variations may occur. Thus, this technique is not suitable for the purposes of this paper, either.

MMCs have evolved as a popular technology for HVDC systems in industry and academia: this trend is confirmed by a search on Scopus, according to which since 2018 (i.e., 15 years from the first inception of this converter [24]), at least 800 papers including "MMC" in their keywords have been published every year. MMCs are also gaining ground as means for integrating renewable energy sources at the SM level. Therefore, developing new and more efficient ways to harvest renewable energy sources through MMCs constitutes a research avenue worth pursuing, which may yield a relevant contribution to the industry sector and academic field. This is the reason why this paper focuses on using MMCs to integrate PV arrays at the SM level through a reduced number of sensors.

Based on the previous introduction, MMCs with a reduced number of sensors do exist. However, it is worth reminding that such solutions with a reduced number of sensors are mostly conceived for SMs based on half-/full-bridge cells and a floating capacitor, and do not contemplate the possibility of integrating PV arrays at the SM level as we do in this paper. Depending on this case, extending the previously-mentioned solutions to SMs with PV arrays may either be impossible or require certain adjustments anyway.

The usage of the EKF for MMC-based PV systems has never been explored before. To fill in this gap, in this paper, we improve the control strategy of three-phase MMC for PV integration in [23] by exploiting an EKF. For each MMC arm, the EKF receives the gate signals and duty cycles of SMs, the arm current, and the voltage across the cascading stack of SMs as inputs. In turn, the voltage and irradiance of each SM are estimated. Other than requiring significantly fewer sensors compared with strategies relying on the knowledge of voltage and current for each PV array, the availability of irradiance estimates allows performing DMPPT more directly, without resorting to P&O methods. Moreover, the gate signals and duty cycles used by the EKF are the outputs of the MMC control strategy, so they are known and available: using them instead of the actual measurements at the SM level reduces MMC cost while retaining comparable efficiency. The EKF-based control strategy is compatible with SMs that include a PV array i.e., a non-linear element that calls for a more complex EKF formulation than [34], which considers only SMs with a floating capacitor and half-bridge cells.

The remainder of this paper is organized as follows. Section II outlines the topology and control scheme of an MMC that can be used to integrate PV plants based on DMPPT and the availability of numerous sensors at the SM level. Section III describes the EKF, and how its usage preserves the functionality of control strategy, while allowing the reliance on much fewer sensors. The simulation results that validate the EKF-based controller are reported in Section IV. Finally, conclusions are drawn in Section V. For ease of reference, in Supplementary Material A, we include a list of all the acronyms and variables used in this paper.

II. THREE-PHASE MMC FOR PV INTEGRATION

This paper focuses on PV integration through a three-phase MMC, and the three-phase MMC-based PV system is shown in Fig. 1.

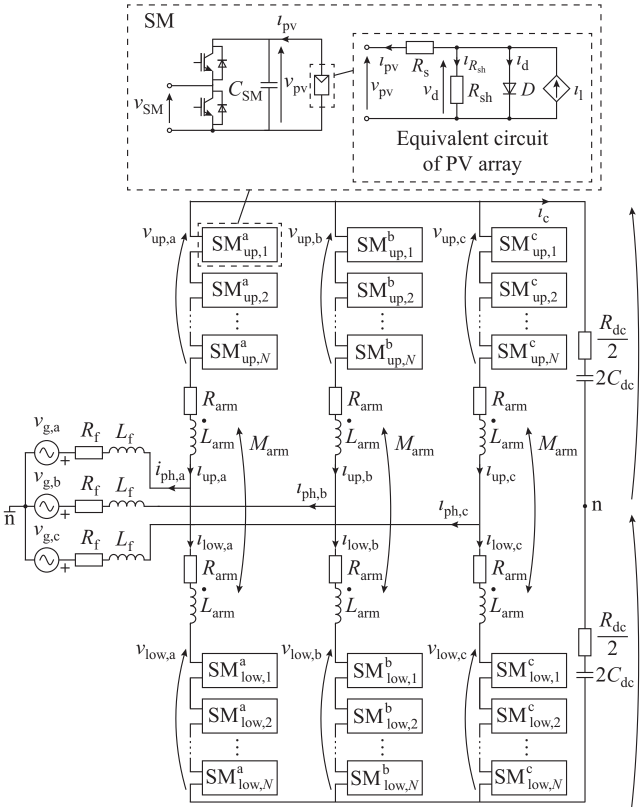

Fig. 1. Three-phase MMC-based PV system.

Different MMC topologies have been proposed in the existing literature, and they can be further classified based on their circuit architecture. According to the classification in [39], this paper focuses on a DSCC structure, which is nonetheless referred hereafter to as MMC for simplicity. The MMC includes three phase legs, each of which comprises two arms. Each arm has a cascaded connection of N SMs, each consisting of a half-bridge cell, a capacitor, and a PV array. The two arms of each phase leg are interconnected through two mutually-coupled inductors L_{arm}. The midpoints between these inductors in each arm constitute the AC terminal of MMC, while the DC terminal includes a capacitor with capacitance C_{dc} and parasitic resistance R_{dc}. If the DC side is not accessible, the three phases are coupled, and any mismatch among the arm power gives rise to circulating current components, both active and reactive, within the converter. However, thanks to the presence of an accessible DC side, this topology achieves leg decoupling and requires only the active circulating current component for managing the arm power. This enhances the overall MMC efficiency [23]. At the steady state, only the sum of circulating currents generated to address the arm power mismatches flows through the DC-side capacitor, thus constituting the current i_{c}.

By analyzing the MMC in Fig. 1, the following holds:

$$\begin{bmatrix} v_{\mathrm{up},k} \\ v_{\mathrm{low},k} \end{bmatrix} = \begin{bmatrix} -1 & 1/2 \\ 1 & 1/2 \end{bmatrix} \begin{bmatrix} v_{\mathrm{g},k} \\ v_{\mathrm{dc}} \end{bmatrix} - \begin{bmatrix} R_{\mathrm{f}}+R_{\mathrm{arm}} & -R_{\mathrm{f}} \\ -R_{\mathrm{f}} & R_{\mathrm{f}}+R_{\mathrm{arm}} \end{bmatrix} \begin{bmatrix} i_{\mathrm{up},k} \\ i_{\mathrm{low},k} \end{bmatrix} - \begin{bmatrix} L_{\mathrm{f}}+L_{\mathrm{arm}} & -L_{\mathrm{f}}+M_{\mathrm{arm}} \\ -L_{\mathrm{f}}+M_{\mathrm{arm}} & L_{\mathrm{f}}+L_{\mathrm{arm}} \end{bmatrix} \frac{\mathrm{d}}{\mathrm{d}t} \begin{bmatrix} i_{\mathrm{up},k} \\ i_{\mathrm{low},k} \end{bmatrix} \tag{1}$$

where $k \in \{a, b, c\}$ is the index of three phases; $v_{\mathrm{up},k}$ and $v_{\mathrm{low},k}$ are the voltages of upper and lower arms, respectively; $v_{\mathrm{g},k}$ is the grid voltage; v_{dc} is the DC-side voltage of MMC; R_{arm}, L_{arm}, and M_{arm} are the arm resistance, arm inductance, and arm mutual inductance, respectively; R_{f} and L_{f} are the output filter resistance and inductance, respectively; and $i_{\mathrm{up},k}$ and $i_{\mathrm{low},k}$ are the currents of upper and lower arms, respectively, which are related to the output phase currents $i_{\mathrm{ph},k}$ and circulating currents $i_{\mathrm{circ},k}$:

$$\begin{bmatrix} i_{\mathrm{ph},k} \\ i_{\mathrm{circ},k} \end{bmatrix} = \begin{bmatrix} 1 & -1 \\ 1/2 & 1/2 \end{bmatrix} \begin{bmatrix} i_{\mathrm{up},k} \\ i_{\mathrm{low},k} \end{bmatrix} \tag{2}$$

By substituting (2) in (1), it is possible to express the arm voltages with the output phase voltage $v_{\mathrm{ph},k}$ and circulating voltages $v_{\mathrm{circ},k}$ as:

$$\begin{bmatrix} v_{\mathrm{up},k} \\ v_{\mathrm{low},k} \end{bmatrix} = \begin{bmatrix} -1 & 1/2 \\ 1 & 1/2 \end{bmatrix} \begin{bmatrix} v_{\mathrm{ph},k} \\ v_{\mathrm{circ},k} \end{bmatrix} \tag{3}$$

$$\begin{bmatrix} v_{\mathrm{ph},k} \\ v_{\mathrm{circ},k} \end{bmatrix} = \begin{bmatrix} 1 & 0 \\ 0 & 1 \end{bmatrix} \begin{bmatrix} v_{\mathrm{g},k} \\ v_{\mathrm{dc}} \end{bmatrix} + \begin{bmatrix} R_{\mathrm{f}}+R_{\mathrm{arm}}/2 & 0 \\ 0 & -2R_{\mathrm{arm}} \end{bmatrix} \begin{bmatrix} i_{\mathrm{ph},k} \\ i_{\mathrm{circ},k} \end{bmatrix} + \begin{bmatrix} L_{\mathrm{f}} & 0 \\ 0 & -2\left(L_{\mathrm{arm}}+M_{\mathrm{arm}}\right) \end{bmatrix} \frac{\mathrm{d}}{\mathrm{d}t} \begin{bmatrix} i_{\mathrm{ph},k} \\ i_{\mathrm{circ},k} \end{bmatrix} \tag{4}$$

The terms $v_{\mathrm{ph},k}$ and $v_{\mathrm{circ},k}$ are among the main variables defined by the MMC control strategy. In particular, $v_{\mathrm{ph},k}$ is used for regulating $i_{\mathrm{ph},k}$, thereby managing the active/reactive power exchange at the AC terminals. Conversely, $v_{\mathrm{circ},k}$ is employed for regulating $i_{\mathrm{circ},k}$, which is crucial for implementing the DMPPT algorithm. As demonstrated in [23], by injecting AC and DC circulating currents, the converter arms can operate at different voltage points while maintaining balanced output power. The AC circulating currents manage the energy between arms belonging to the same phase, while the DC components regulate the energy among the three phase legs. Additionally, the voltage $v_{\mathrm{circ},k}$ also contains the DC zero-sequence component, which is necessary to enable the arms to synthesize only positive voltages, given that they are based on half-bridge cells. Lastly, by adopting a sorting algorithm based on the individual SM voltages, it is possible to regulate the power produced by each integrated PV array.

A. PV Array Model

The PV arrays integrated at the SM level in the MMC-based PV system (see Fig. 1) are modeled by:

$$\begin{cases} v_{\mathrm{d}}=R_{\mathrm{s}} i_{\mathrm{pv}}+v_{\mathrm{pv}}=R_{\mathrm{s,ref}} \dfrac{N_{\mathrm{ser}}}{N_{\mathrm{par}}} i_{\mathrm{pv}}+v_{\mathrm{pv}} \\ i_{\mathrm{pv}}=i_{\mathrm{l}}-i_{\mathrm{d}}-i_{R_{\mathrm{sh}}} \\ i_{\mathrm{l}}=\dfrac{G}{G_{\mathrm{ref}}} N_{\mathrm{par}}\left[i_{\mathrm{l,ref}}+\alpha_{i_{\mathrm{sc}}}\left(T-T_{\mathrm{ref}}\right)\right] \\ i_{\mathrm{d}}=i_0\left(\mathrm{e}^{\frac{v_{\mathrm{d}}}{v_T}}-1\right)=i_0\left(\mathrm{e}^{\frac{v_{\mathrm{d}}}{v_{T_{\mathrm{ref}}} N_{\mathrm{ser}}} \frac{T_{\mathrm{ref}}}{T}}-1\right) \\ i_0=i_{0,\mathrm{ref}} N_{\mathrm{par}}\left(\dfrac{T}{T_{\mathrm{ref}}}\right)^3 \mathrm{e}^{\left(\frac{E_{\mathrm{g,ref}}}{k_1 T_{\mathrm{ref}}}-\frac{E_g}{k_1 T_{\mathrm{ref}}}\right)} \\ E_{\mathrm{g}}=E_{\mathrm{g,ref}}\left[\left(T-T_{\mathrm{ref}}\right) \dfrac{\mathrm{d} E}{\mathrm{d} T}+1\right] \\ i_{R_{\mathrm{sh}}}=\dfrac{v_{\mathrm{d}}}{R_{\mathrm{sh}}}=\dfrac{v_{\mathrm{d}}}{R_{\mathrm{sh,ref}} \dfrac{G_{\mathrm{ref}}}{G} \dfrac{N_{\mathrm{ser}}}{N_{\mathrm{par}}}} \end{cases} \tag{5}$$

where v_{pv} and i_{pv} are the voltage and current of PV array, respectively; v_{d} and i_{d} are the diode voltage and current, respectively; i_{l} is the light-generated current; $i_{R_{\mathrm{sh}}}$ is the current flowing through resistor R_{sh}; T and G are the temperature and irradiance of SM, respectively; v_T is the voltage at temperature T; i_0 is the diode saturation current; and E_{g} is the energy bandgap. The other PV array parameters are listed in Table III.

TABLE III
PV ARRAY PARAMETERS

Description	Symbol	Value
Number of PV modules in series	N_{ser}	4
Number of PV modules in parallel	N_{par}	2
Series resistance at reference irradiance and temperature	$R_{\mathrm{s,ref}}$	0.394 Ω
Shunt resistance at reference irradiance and temperature	$R_{\mathrm{sh,ref}}$	313.06 Ω
Reference irradiance	G_{ref}	1000 W/m^2
Reference temperature	T_{ref}	298.15 K
Temperature coefficient of short-circuit current	$\alpha_{i_{\mathrm{sc}}}$	0.008 A/K
Light-generated current at reference irradiance and temperature	$i_{\mathrm{l,ref}}$	7.865 A
Ideal factor parameter	$v_{T_{\mathrm{ref}}}$	1.513 V
Reference diode reverse saturation current	$i_{0,\mathrm{ref}}$	2.927×10^{-10} A
Energy bandgap at reference temperature	$E_{\mathrm{g,ref}}$	1.121 V
Boltzmann's constant	k_1	8.617×10^{-5} V/K
Temperature dependence of energy bandgap	$\mathrm{d}E/\mathrm{d}T$	-2.68×10^{-4} K^{-1}

B. Converter Control Strategy

Figure 2(a) depicts the converter control structure, which is extensively detailed in [23]. Hereafter, we recap only its key features, which are instrumental to understand the benefits introduced by the EKF-based control strategy.

This control strategy includes three main subsystems: the grid, circulating, and modulation controllers. The grid controller manages the active/reactive power exchanges based on grid requirements. In this paper, it is assumed for simplicity that the system always injects the maximum available power from the PV arrays and delivers no reactive power (i.e., the reference q-axis output phase current $i_{\mathrm{ph},q}^*$ is zero in Fig. 2). The circulating controller regulates the average voltage of each arm at its average MPP and keeps the power injected into the grid balanced. Lastly, the modulation controller activates the SMs of each arm needed to synthesize the reference voltage and ensure that all PV arrays operate at their MPPs.

The grid voltage controller (①) defines the reference d-axis output phase current (i.e., $i_{\mathrm{ph},d}^*$) by tracking the DC-side voltage to the mean value of reference MPP voltages, given by:

$$V_{\mathrm{dc}}^*=\frac{1}{6} \sum_{k \in\{\mathrm{a,b,c}\}}\left(\sum_{j=1}^N v_{\mathrm{pv,up},k,j}^*+\sum_{j=1}^N v_{\mathrm{pv,low},k,j}^*\right) \tag{6}$$

where j and N are the index and number of SMs per arm, respectively; and $v_{\mathrm{pv,up},k,j}^*$ and $v_{\mathrm{pv,low},k,j}^*$ are the reference MPP voltages for each SM in the upper and lower arms, respectively. Hereafter, variables with the symbol $*$ are reference values.

Subsequently, the grid current controller (②) regulates the d- and q-axis output phase currents $\boldsymbol{i}_{\mathrm{ph},dq}$ through PI regulators, providing $v_{\mathrm{ph},k}^*$ as output. The Park transformations in this subsystem rely on the grid voltage angle θ_{g}, which is determined by a phase-locked loop (PLL).

The AC and DC circulating controllers define the reference AC and DC circulating voltages (i.e., $v_{\mathrm{cir},k}^{\mathrm{ac}*}$ and $v_{\mathrm{cir},k}^{\mathrm{dc}*}$) for injecting the reference AC and DC circulating currents $i_{\mathrm{circ},k}^{\mathrm{ac}*}$ and $i_{\mathrm{circ},k}^{\mathrm{dc}*}$, respectively. Thus, the reference circulating voltage is given by $v_{\mathrm{circ},k}^*=v_{\mathrm{circ},k}^{\mathrm{ac}*}+v_{\mathrm{circ},k}^{\mathrm{dc}*}$.

The AC circulating voltage controller (③) determines $i_{\mathrm{circ},k}^{\mathrm{ac}*}$ by tracking the difference between the reference MPP voltages in the upper and lower arms $V_{\mathrm{diff},k}^*$ through an outer loop for phase k:

$$V_{\mathrm{diff},k}^*=\sum_{j=1}^N v_{\mathrm{pv,up},k,j}^*-\sum_{j=1}^N v_{\mathrm{pv,low},k,j}^* \tag{7}$$

The sequence components of d- and q-axis reference AC circulating currents $\boldsymbol{i}_{\mathrm{circ},dq,+}^{\mathrm{ac}*}$, $\boldsymbol{i}_{\mathrm{circ},dq,-}^{\mathrm{ac}*}$, and $\boldsymbol{i}_{\mathrm{circ},dq,0}^{\mathrm{ac}*}$ are defined from $i_{\mathrm{circ},k}^{\mathrm{ac}*}$ and are regulated by the AC circulating current controller (④) with additional PI regulators. These regulators output the sequence components of d- and q-axis reference AC circulating voltages $\boldsymbol{v}_{\mathrm{circ},dq,+}^{\mathrm{ac}*}$, $\boldsymbol{v}_{\mathrm{circ},dq,-}^{\mathrm{ac}*}$, and $\boldsymbol{v}_{\mathrm{circ},dq,0}^{\mathrm{ac}*}$. By applying the inverse Park transformation, the corresponding sequence voltages in the abc frame $v_{\mathrm{circ},k,+}^{\mathrm{ac}*}$, $v_{\mathrm{circ},k,-}^{\mathrm{ac}*}$, and $v_{\mathrm{circ},k,0}^{\mathrm{ac}*}$ are obtained, from which $v_{\mathrm{circ},k}^{\mathrm{ac}*}$ is then retrieved. The Park transformations in this subsystem rely on the angle of reference output phase voltages $\theta_{v_{\mathrm{ph}}}$, determined by another PLL. By doing so, the performance of AC circulating controller is improved compared with its implementation in the grid reference frame (i.e., using θ_{g} instead). It is worth noting that the accessible DC-side in Fig. 1 allows decoupling the MMC legs during arm power mismatches, as the AC circulating currents are generated only in the affected phases and will close their path through the DC capacitor without impacting other legs.

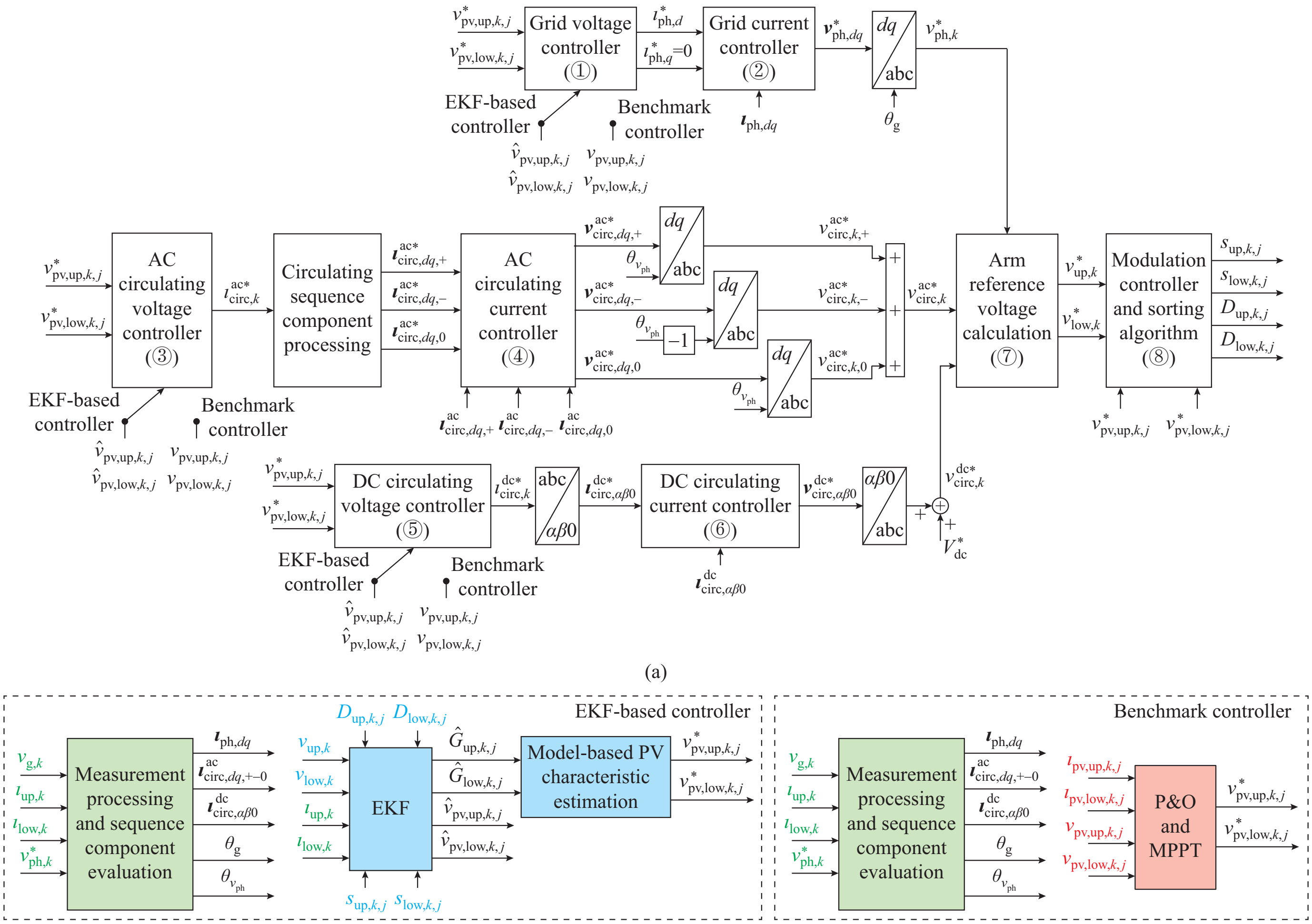

Fig. 2. Control structure and measurement process. (a) Control structure. (b) Measurement process in the case of EKF-based controller and benchmark controller [23].

The DC circulating voltage controller (⑤) determines $i^{dc*}_{circ,k}$ by tracking the differences between the sums of SM voltages of two legs (i.e., $V^*_{diff,a-b}$ and $V^*_{diff,a-c}$) to their respective MPP values:

$$\begin{cases} V^*_{diff,a-b}=V^*_{dc,a}-V^*_{dc,b} \\ V^*_{diff,a-c}=V^*_{dc,a}-V^*_{dc,c} \end{cases} \tag{8}$$

$$V^*_{dc,k}=\frac{\sum_{j=1}^{N} v^*_{pv,up,k,j}+\sum_{j=1}^{N} v^*_{pv,low,k,j}}{2} \tag{9}$$

Two PI regulators are used, exploiting the fact that the sum of three DC circulating currents must equal zero. From the outputs of these regulators, the reference DC circulating currents $i^{dc*}_{circ,k}$ are derived. They are transformed into the $\alpha\beta 0$ frame (i.e., $\boldsymbol{i}^{dc*}_{circ,\alpha\beta 0}$) and controlled in the DC circulating current controller (⑥) through additional PI regulators, outputting the reference DC circulating voltage in the $\alpha\beta 0$ frame $\boldsymbol{v}^{dc*}_{circ,\alpha\beta 0}$. By the inverse $\alpha\beta 0$-abc transformation and adding V^*_{dc}, the reference DC circulating voltages $v^{dc*}_{circ,k}$ are retrieved.

Through (3) and by exploiting the fact that $v^*_{circ,k}=v^{ac*}_{circ,k}+v^{dc*}_{circ,k}$, the reference voltages of upper and lower arms $v^*_{up,k}$ and $v^*_{low,k}$ are computed (⑦). Then, the modulation controller (⑧) selects which SM to activate to synthesize $v^*_{up,k}$ and $v^*_{low,k}$, thus determining the gate signals (i.e., $s_{up,k,j}$ and $s_{low,k,j}$) and duty cycles (i.e., $D_{up,k,j}$ and $D_{low,k,j}$) of each SM. A sorting algorithm (⑧) is adopted, which activates the SM based on the current direction of each arm and the deviation of SM capacitor voltages from their theoretical optimum, as described in [30]. This allows the separate control of PV arrays integrated into each SM, enabling the operation at different power points based on their irradiances. Once the SMs to be activated are determined, $v^*_{up,k}$ and $v^*_{low,k}$ are synthesized through phase-disposition pulse width modulation (PWM).

As will be detailed in Section III-C, to ensure the optimal operation of the MMC-based PV system, it is crucial to define the reference MPP voltages for each SM (i.e., $v^*_{pv,up,k,j}$ and $v^*_{pv,low,k,j}$). These values are commonly derived through the P&O method. However, this method requires numerous sensors, as it uses the current and voltage of each PV array as inputs. In the control strategy proposed in this work, an EKF is implemented to reduce the number of measurements needed while maintaining optimal system performance.

Figure 2(b) shows the measurement process in the case of EKF-based controller and benchmark controller, where the measurements and control signals common to both controllers are coloured in green, and the measurements and control signals exclusively required by the benchmark controller and EKF-based controller are highlighted in red and blue, respectively.

III. EKF

A. EKF in a Nutshell

The EKF [40] allows estimating the state variables of a discrete, non-linear, and dynamic system through the knowledge of its inputs and outputs in time, as well as of a model that captures its behavior with the discrete-time equations:

$$\begin{cases} \boldsymbol{x}_m = \boldsymbol{f}(\boldsymbol{x}_{m-1}, \boldsymbol{u}_m) + \boldsymbol{w}_m \\ \boldsymbol{y}_m = \boldsymbol{h}(\boldsymbol{x}_m, \boldsymbol{u}_m) + \boldsymbol{v}_m \end{cases} \tag{10}$$

where the subscript m indicates a specific time step, which has been ommitted in Fig. 1 for simplicity; $\boldsymbol{f}$ and $\boldsymbol{h}$ are the possibly non-linear vector functions; $\boldsymbol{x}$, $\boldsymbol{u}$, and $\boldsymbol{y}$ are the system state variable, input, and output vectors, respectively; and $\boldsymbol{w}$ and $\boldsymbol{v}$ are the process and measurement noise vectors, respectively.

The working principle of the EKF, as depicted in Fig. 3, can be explained as follows. Hereafter, variables with the symbol $\hat{}$ are estimated values, while those without it are measured/true ones.

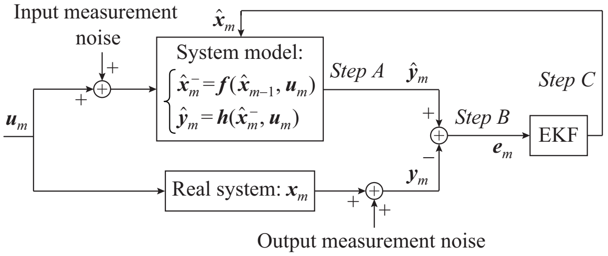

Fig. 3. Working principle of EKF.

Since state variables are unknown, they can only be assumed. At each time step m, based on an assumed set of state variables $\hat{\boldsymbol{x}}_{m-1}$ and inputs $\boldsymbol{u}_m$, *a* priori predicted state variables $\hat{\boldsymbol{x}}_m^-$ and outputs $\hat{\boldsymbol{y}}_m$ (*step A*) are provided through the system model. If the system model is accurate and the measurement noise is low enough, the differences between $\hat{\boldsymbol{y}}_m$ and $\boldsymbol{y}_m$ (i.e., the prediction error $\boldsymbol{e}_m$) are mostly due to deviations between the state variable estimates and their true values (*step B*). The EKF exploits this mismatch to update the state variable estimates and provide a set of *a* posteriori predicted state variables $\hat{\boldsymbol{x}}_m$ (*step C*). The above steps are repeated at each time instant. In the light of this, the EKF iteratively resorts to two phases to update the state variable estimates: a prediction phase and a correction phase.

To initialize the EKF, it is necessary to specify an initial assumption of the state variables $\boldsymbol{x}_0$ and covariance matrix of state estimation errors $\boldsymbol{P}_0$, as well as the covariance matrices of process and measurement noises $\boldsymbol{Q}$ and $\boldsymbol{R}$.

B. EKF for MMC-based Three-phase PV Systems

We now show how we applied the EKF to an MMC used to integrate PV arrays at the SM level, thereby enabling DMPPT. The proposed EKF is replicated in each arm of the MMC. For simplicity, however, hereafter we consider a single MMC arm with a given number N of SMs (or PV arrays), and use $\imath_{\text{arm}}$ and v_{arm} to respectively refer to the current and voltage across the stack of SM of that given arm. In this implementation, the vectors $\boldsymbol{x}$, $\boldsymbol{u}$, and $\boldsymbol{y}$ and the functions $\boldsymbol{f}$ and $\boldsymbol{g}$ specialize as follows. For ease of notation, the variables in this section lack subscripts up/low and k indicating upper/lower arm and phase, respectively, while the subscripts m and j are used.

1) The predicted state variables $\hat{\boldsymbol{x}}_m \in \mathbb{R}^{2N\times 1}$ collects the voltage v_{pv} and irradiance G of each PV array in a given arm. In particular, $\hat{\boldsymbol{x}}_m$ is organized as: $\left[\hat{v}_{\text{pv},1_m}, \hat{v}_{\text{pv},2_m}, ..., \hat{v}_{\text{pv},N_m}, \hat{G}_{1_m}, \hat{G}_{2_m}, ..., \hat{G}_{N_m}\right]^{\text{T}}$.

2) The input vector $\boldsymbol{u}_m \in \mathbb{R}^{(2N+1)\times 1}$ includes the arm current $\imath_{\text{arm}}$, the duty cycles D, and gate signals s of each SM. $\boldsymbol{u}_m$ is organized as: $\left[\imath_{\text{arm}_m}, D_{1_m}, D_{2_m}, ..., D_{N_m}, s_{1_m}, s_{2_m}, ..., s_{N_m}\right]^{\text{T}}$. The reason why both duty cycles and gate signals are used despite having similar meanings is explained in Section IV.

3) The output $\boldsymbol{y}_m \in \mathbb{R}^1$ (i.e., a scalar value) is the arm voltage v_{arm_m} across the stack of SMs in the MMC arm.

The entries of $\boldsymbol{f}$: $\mathbb{R}^{2N} \rightarrow \mathbb{R}^{2N}$ can be expressed as:

$$\boldsymbol{f} = \begin{bmatrix} \hat{v}_{\text{pv},1_{m-1}} + \dfrac{\Delta t}{C_{\text{SM}}}\left(\imath_{\text{arm}_m} D_{1_m} + \imath_{\text{pv}}\left(\hat{v}_{\text{pv},1_{m-1}}, \hat{G}_{1_{m-1}}\right)\right) \\ \hat{v}_{\text{pv},2_{m-1}} + \dfrac{\Delta t}{C_{\text{SM}}}\left(\imath_{\text{arm}_m} D_{2_m} + \imath_{\text{pv}}\left(\hat{v}_{\text{pv},2_{m-1}}, \hat{G}_{2_{m-1}}\right)\right) \\ \vdots \\ \hat{v}_{\text{pv},N_{m-1}} + \dfrac{\Delta t}{C_{\text{SM}}}\left(\imath_{\text{arm}_m} D_{N_m} + \imath_{\text{pv}}\left(\hat{v}_{\text{pv},N_{m-1}}, \hat{G}_{N_{m-1}}\right)\right) \\ \hat{G}_{1_{m-1}} \\ \hat{G}_{2_{m-1}} \\ \vdots \\ \hat{G}_{N_{m-1}} \end{bmatrix} \tag{11}$$

where Δt is the period between two consecutive time steps (i.e., m and $m-1$); and C_{SM} is the SM capacitance.

The last N entries of $\boldsymbol{f}$ are introduced to allow the EKF to estimate generic parameters (i.e., irradiance levels of the PV array). Indeed, since they are not state variables strictly speaking, their estimates remain the same in the prediction phase, and thus can only change in the correction phase. On the contrary, the first N entries of $\boldsymbol{f}$ describe the charging/discharging of each SM capacitor in a discretized form by taking into account that they depend on the arm current, duty cycle, and current of PV array $\imath_{\text{pv}}$. This latter variable is computed through the function $\imath_{\text{pv}}\left(\hat{v}_{\text{pv},j_m}, \hat{G}_{j_m}\right)$: $\mathbb{R}^2 \rightarrow \mathbb{R}^1$ based on the estimated voltage and irradiance of each SM.

By examining (5), it is not possible to write an explicit relationship among $\imath_{\text{pv}}$, v_{pv}, and G for a single SM at the first glance. Indeed, according to the second row of (5), $\imath_{\text{pv}}$ is partly related with $\imath_{\text{d}}$ and $\imath_{R_{\text{sh}}}$, both of which depend on v_{d}.

However, as shown in the first row of (5), v_{d} is determined by v_{pv} and the voltage across R_{s}, which ultimately depends on the current $\imath_{\mathrm{pv}}$ that we would like to determine. A way to circumvent this issue is to in resort to the Lambert (or product-log) function $W(x)$ [41], through which $\imath_{\mathrm{pv},j_m}$ can be written in an explicit form as:

$$\imath_{\mathrm{pv},j_m}=\imath_{\mathrm{pv}}\left(\hat{v}_{\mathrm{pv},j_m},\hat{G}_{j_m}\right)=\frac{R_{\mathrm{sh},j_m}\left(\imath_{\mathrm{ph},j_m}+\imath_0\right)-\hat{v}_{\mathrm{pv},j_m}}{R_{\mathrm{sh},j_m}+R_{\mathrm{s}}}-\frac{v_T}{R_{\mathrm{s}}}W\left(\frac{R_{\mathrm{s}}R_{\mathrm{sh},j_m}\imath_0}{\left(R_{\mathrm{sh},j_m}+R_{\mathrm{s}}\right)v_T}\mathrm{e}^{\frac{\hat{v}_{\mathrm{pv}}R_{\mathrm{sh},j_m}+R_{\mathrm{sh},j_m}R_s\left(\imath_0+\imath_{\mathrm{ph},j_m}\right)}{\left(R_{\mathrm{sh},j_m}+R_s\right)v_T}}\right) \tag{12}$$

where the dependency of $\imath_{\mathrm{ph},j_m}$ and R_{sh,j_m} on irradiance $\hat{G}_{j_m}$ is kept implicit for ease of notation but can be found from (5).

The function $\boldsymbol{h}\colon \mathbb{R}^N \rightarrow \mathbb{R}^1$ is described as:

$$\boldsymbol{h}=\left[\hat{v}_{\mathrm{arm}_m}\right]=\left[\hat{v}^{-}_{\mathrm{pv},1_m},\hat{v}^{-}_{\mathrm{pv},2_m},\ldots,\hat{v}^{-}_{\mathrm{pv},N_m}\right]\left[s_{1_m},s_{2_m},\ldots,s_{N_m}\right]^{\mathrm{T}} \tag{13}$$

The function $\boldsymbol{h}$, characterized by a single entry, allows predicting the voltage v_{arm_m}, which is compared with its measured counterpart at each time step in the correction phase.

Based on the above variables and functions, the EKF estimates the SM voltage and irradiance at each time step, separated from one another by a period Δt. This structure is replicated for each MMC arm. For instance, in the case of the MMC upper arm of phase a, $\hat{\boldsymbol{x}}_m$, $\boldsymbol{u}_m$, and $\boldsymbol{y}_m$ become:

$$\begin{cases}\hat{\boldsymbol{x}}_m=\left[\hat{v}_{\mathrm{pv,\,up,\,a},\,1_m},\ldots,\hat{v}_{\mathrm{pv,\,up,\,a},\,N_m},\hat{G}_{\mathrm{up,\,a},\,1_m},\ldots,\hat{G}_{\mathrm{up,\,a},\,N_m}\right]^{\mathrm{T}}\\ \boldsymbol{u}_m=\left[\imath_{\mathrm{up}_m,\mathrm{a}},D_{\mathrm{up,\,a},\,1_m},\ldots,D_{\mathrm{up,\,a},\,N_m},s_{\mathrm{up,\,a},\,1_m},\ldots,s_{\mathrm{up,\,a},\,N_m}\right]^{\mathrm{T}}\\ \boldsymbol{y}_m=\left[v_{\mathrm{up}_m,\mathrm{a}}\right]\end{cases} \tag{14}$$

Given the predicted state variables $\hat{\boldsymbol{x}}_m$, the integrated PV arrays can be individually controlled to extract their maximum power. Specifically, by using the irradiance estimation, knowing the PV array temperature, and exploiting the characteristics of the PV array reported in (5), $v^*_{\mathrm{pv,\,up},k,j}$ and $v^*_{\mathrm{pv,\,low},k,j}$ can be determined. Consequently, the reference arm, leg, and SM voltages can be retrieved, as described in Section II-B, allowing each PV array to be regulated at its optimal average voltage.

The interested reader can refer to Supplementary Materials B and C for details about the Lambert function and EKF, which are omitted here for space reasons.

C. EKF-based and Benchmark Controllers: A Comparison

As shown in Fig. 2(b), the EKF-based controller and benchmark controller based on the P&O method [23] determine $v^*_{\mathrm{pv,\,up},k,j}$ and $v^*_{\mathrm{pv,\,low},k,j}$ at each time step. These voltages are then used as inputs of other blocks in Fig. 2(a), which are common to the two controllers. The difference is the process for determining $v^*_{\mathrm{pv,\,up},k,j}$ and $v^*_{\mathrm{pv,\,low},k,j}$. Indeed, the EKF-based controller estimates the voltage and irradiance of each SM. Then, the MPP of each SM is determined based on the PV array characteristics. Conversely, the benchmark controller finds the MPP by performing voltage perturbations on each PV array and measuring their exchanged power.

Compared with the benchmark controller, the EKF-based controller is more flexible, as it allows PV arrays operating at points possibly different from the MPP by exploiting its characteristic curve. For instance, this may be required when the inverter-based PV systems must reduce their output power to comply with stringent grid codes. If the P&O method were used instead, the modified control strategies would be necessary to determine the PV operating points corresponding to a lower power output.

Furthermore, another key difference between the two controllers is the number of sensors required. These inputs are needed for implementing two main converter control blocks: the grid and circulating controllers. The necessary measurements include the voltages at the point of connection ($v_{\mathrm{g},k}$) and the arm currents ($\imath_{\mathrm{up},k}$ and $\imath_{\mathrm{low},k}$), which are essential for determining the output phase and circulating currents. Regarding the control signals, the reference output phase voltage ($v^*_{\mathrm{ph},k}$) is needed to derive $\theta_{v_{\mathrm{ph}}}$, which is in turn used for generating the AC circulating voltages.

The inputs required by the two controllers are not the same because, as already stated, they derive the reference SM voltages in different ways.

P&O methods (used by the benchmark controller) use the current and voltage of each SM to compute their power exchange, which is exploited to find the MPP while performing voltage perturbations. Thus, the measurements required in this case increase with the number of SMs in the MMC, while no other control signal is needed.

On the contrary, the number of sensors needed for the EKF depends solely on the number of converter arms (i.e., six in the case of MMC), regardless of how many SMs are stacked inside them. Specifically, the EKF-based controller uses the arm voltage and current as well as the duty cycles and gate signals of each SM in one arm (i.e., control signals) as inputs. These inputs are exploited by the EKF to estimate the voltage and irradiance of each SM. It is worth noting that sensors are actually needed only for arm voltages and currents, since control signals are generated automatically during converter operation (and, as such, ad hoc sensors are not needed for their retrieval). Thus, using more control signals is not disadvantageous for the actual implementation of EKF-based controller. Instead, reducing the number of required sensors is economically advantageous, especially in the case of power plants with a large number of SMs.

To recap, the benchmark controller uses $9+2\times N\times 6$ measurements and 3 control signals, while the EKF-based controller uses 15 measurements and $3+2\times N\times 6$ control signals.

IV. SIMULATION RESULTS

In this section, the validity of EKF-based controller is demonstrated by simulating the network in Fig. 1 in the time domain on MATLAB Simulink. The test bench consists of a 20 kVA MMC-based PV system, with $N=12$ SMs per arm connected to a 400 V electric grid. The PV array parameters and MMC system are shown in Tables III and IV, respectively. The EKF-based controller is implemented by adopting the parameters shown in Table V.

TABLE IV
MMC SYSTEM PARAMETERS

Description	Symbol	Value
Rated plant power	P_{r}	20 kW
Rated grid phase voltage	v_{g}	230.9 V
Nominal peak arm voltage	$v_{\mathrm{arm}}^{\mathrm{peak}}$	823.11 V
Nominal peak arm current	$\imath_{\mathrm{arm}}^{\mathrm{peak}}$	20.41 A
Output filter resistance	R_{f}	140 mΩ
Output filter inductance	L_{f}	3.9 mH
Arm resistance	R_{arm}	5 mΩ
Arm inductance	L_{arm}	1 mH
Arm mutual inductance	M_{arm}	0.99 mH
SM capacitance	C_{SM}	50 mF
DC-side capacitance	C_{dc}	5 mF
DC-side resistance	R_{dc}	15 mΩ
Number of SMs per arm	N	12
Switching frequency	f_{sw}	9 kHz
Execution frequency of EKF-based controller	f_{EKF}	6 kHz

TABLE V
PARAMETERS OF EKF-BASED CONTROLLER

Symbol	Value
$\boldsymbol{R}$	$\left[1\times 10^{-4}\right]$
$\boldsymbol{Q}$	$\operatorname{diag}\left(\boldsymbol{q}_1,\boldsymbol{q}_2\right)$
$\boldsymbol{P}_0$	$10^{-10}\boldsymbol{I}_{24\times 24}$
$\hat{\boldsymbol{x}}_0$	$\boldsymbol{x}_{0_{\mathrm{true}}}\left(1+\mathcal{N}\left(0,0.01\right)\right)$

Note: $\boldsymbol{q}_1=10^{-12}\boldsymbol{I}_{12\times 12}$, and $\boldsymbol{I}$ is the identical matrix; $\boldsymbol{q}_2=10^{-10}\boldsymbol{I}_{12\times 12}$; $\boldsymbol{x}_{0_{\mathrm{true}}}$ is the vector of initial true state variables; and $\mathcal{N}(\mu,\sigma)$ is a Gaussian distribution with mean μ and standard deviation σ.

For the sake of simplicity, the irradiance variations are simulated only in the upper arm of phase a, while other arms operate under standard test conditions. Note that this does not compromise the operation of the whole system. Indeed, the EKF-based controllers are implemented separately in every converter arm. Each of them operates independently because they require the arm voltage and current as well as the duty cycles and gate signals of each SM in one arm as inputs.

The following two different scenarios are simulated.

1) In scenario A, the SMs in the upper arm of phase a operate at the same irradiance of 1 kW/m^2, which is changed uniformly in a step-wise manner to 0.4 kW/m^2 at 5 s to consider natural changes in irradiance over time.

2) In scenario B, the SMs in the upper arm of phase a operate at different irradiances from the beginning, which change unevenly in a step-wise manner at 5 s, as shown in Table VI. This scenario is introduced to test the performance of the EKF-based controller under the extreme condition, where partial shading phenomena affect each SM in one arm.

In both scenarios, all PV arrays work at the ambient temperature of 298.15 K (i.e., 25 °C), assumed to be known.

TABLE VI
IRRADIANCES OF SMS IN UPPER ARM OF PHASE a (SCENARIO B)

SM No.	G (kW/m^2)	
	$0\ \mathrm{s}<t<5\ \mathrm{s}$	$5\ \mathrm{s}<t<10\ \mathrm{s}$
1	1.00	0.50
2	0.73	0.25
3	0.25	0.30
4	0.60	0.70
5	0.54	0.80
6	0.35	1.00
7	0.65	0.25
8	0.95	0.45
9	0.80	0.75
10	0.90	0.67
11	0.51	0.20
12	0.16	0.95

Noises are added to the measurements of arm voltages and currents, i.e., $v_{\mathrm{up},k}=v_{\mathrm{arm}}^{\mathrm{peak}}\left(1+\mathcal{N}\left(0,0.025\right)\right)$ and $\imath_{\mathrm{up},k}=\imath_{\mathrm{arm}}^{\mathrm{peak}}\left(1+\mathcal{N}\left(0,0.05\right)\right)$, respectively. Noises are also added in a similar fashion for the homologous variables in the other arms. The matrices $\boldsymbol{R}$, $\boldsymbol{Q}$, and $\boldsymbol{P}_0$ are listed in Table V. Their tuning has heuristically proven to yield good performances of the EKF-based controller.

For what concerns the initial estimates of the state variables $\boldsymbol{x}_0$, the following holds. Analogously to the measurements, the initial estimates of the SM capacitor voltages are selected by adding a Gaussian noise with zero mean and standard deviation equal to 10% to their true initial values. The same is done for the initial estimates of the SM irradiances. This is made to consider the possibility that the EKF-based controller may start operating with an initial estimation error. Nonetheless, its estimates are expected to converge to their true values after some time.

All simulations are carried out by adopting a fixed integration time step of 1 μs. In principle, the EKF-based controller should update its output estimates at the same rate. However, given the computational capabilities of modern microprocessors, this value would be excessive and unpractical in real applications. To address this issue, we let the EKF-based controller work at a reduced rate of $f_{\mathrm{EKF}}=6$ kHz, that is, the estimated outputs are updated only every $\Delta t\approx 0.166$ ms. Therefore, they remain constant at time steps between consecutive multiple values of Δt.

This choice has a notable consequence on the EKF-based controller. Indeed, by down-sampling data, sudden jumps in the gate signals at time steps between consecutive multiple values of Δt are unnoticed. Being "average" values by definition, duty cycles are more robust to data decimation than gate signals. Thus, using duty cycles rather than gate signals in (11) leads to lower errors when the EKF-based controller updates the SM capacitor voltages in the prediction phase. However, the duty cycles cannot replace the gate signals in (13) as the arm voltage computation is sensitive to the dynamic behavior of gate signals. These features explain why the EKF-based controller adopts duty cycles in the prediction phase and gate signals in the correction phase.

Lastly, it is worth specifying that scenarios A and B have been simulated twice. In one set of simulations, the EKF-based controller is used, while in the other set, the benchmark controller based on the P&O method [23] is considered. Moreover, it was intentionally assumed that the benchmark controller has full availability to measurements at the SM level and is devoid of measurement errors and downsampling as well as other real-world limitations. Many conventional control methods intentionally overlook these factors, which are significant in the context of the EKF-based controller. Thus, the following comparison between the results in each simulation set is meant to highlight how close the EKF-based controller operates compared with a somewhat ideal scenario.

A. Scenario A: SMs Under Uniform Irradiance Conditions

In this scenario, the EKF-based controller is tested when the SMs in the upper arm of phase a work under uniform irradiance conditions. Simulation results in scenario A are reported in Fig. 4.

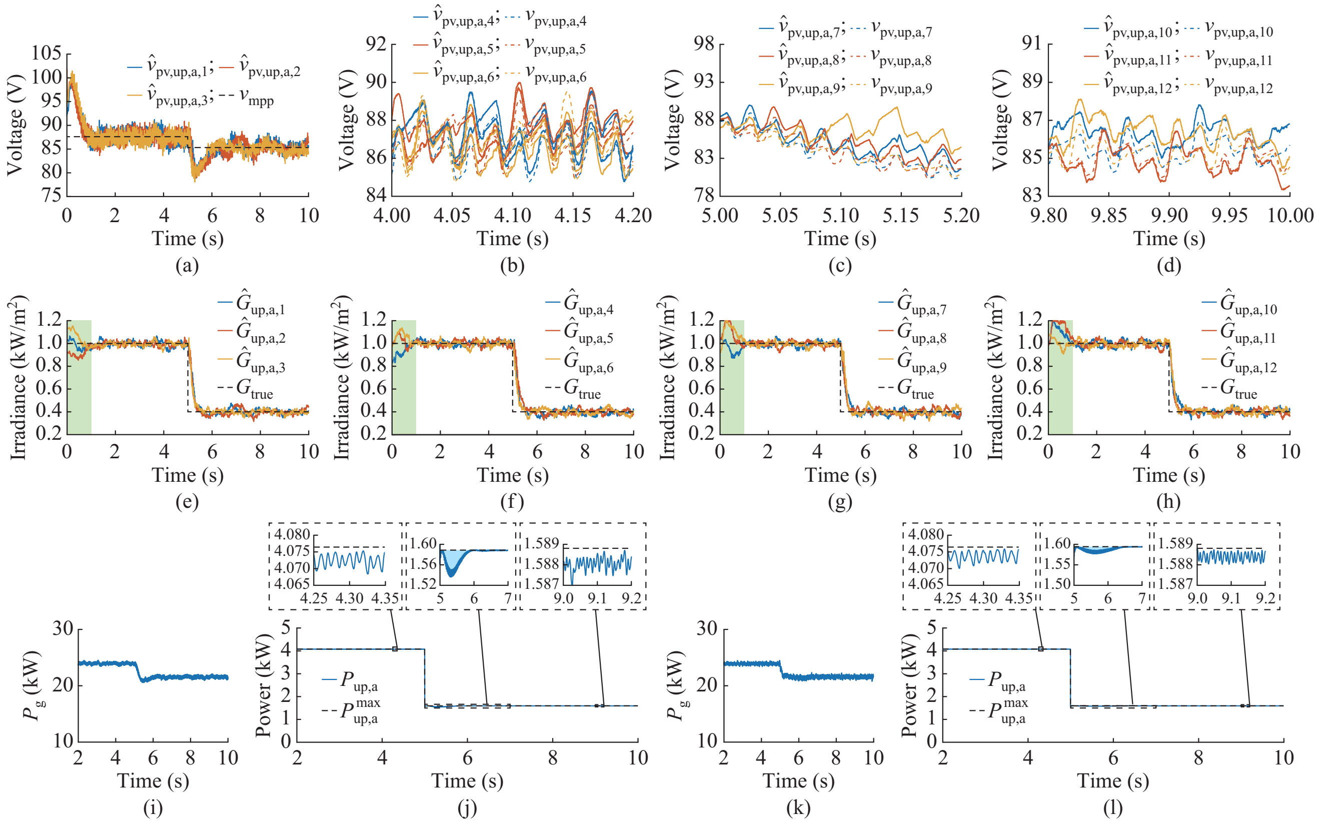

Fig. 4. Simulation results in scenario A. (a) Estimated voltages of SMs 1-3 over entire simulation time. (b) Estimated and actual voltages of SMs 4-6 during 4.0-4.2 s. (c) Estimated and actual voltages of SMs 7-9 during 5.0-5.2 s. (d) Estimated and actual voltages of SMs 10-12 during 9.8-10.0 s. (e) Estimated irradiances of SMs 1-3. (f) Estimated irradiances of SMs 4-6. (g) Estimated irradiances of SMs 7-9. (h) Estimated irradiances of SMs 10-12. (i) P_g using EKF-based controller. (j) $P_{up,a}$ using EKF-based controller. (k) P_g using benchmark controller. (l) $P_{up,a}$ using benchmark controller.

Initially, all the SMs operate at 1 kW/m^2. After 5 s, their irradiance decreases to 0.4 kW/m^2. To test the effectiveness of the EKF-based controller and highlight its robustness, the initial estimates of the SM irradiances and voltages are intentionally set differently from their true values. After a short transient, the SM voltages (for clarity, only three of the twelve SM voltages are reported in Fig. 4(a)) stabilize at, on average, their theoretical optimal values v_{mpp}. This is attributed to the accurate irradiance estimates. Indeed, as shown in Fig. 4(e)-(h), the estimated irradiances converge to the reference values G_{true} after a short transient highlighted in green.

After 5 s, SMs are subject to the same step change in irradiance. Despite this, the estimated irradiances stabilize in less than 1 s (as shown in Fig. 4(e)-(h)), and the SM voltages quickly settle under the steady-state condition corresponding to the new MPP (as shown in Fig. 4(a)). Figure 4(b)-(d) compares the estimated and actual SM voltages during specific time intervals, including transient and steady-state operation. The discrepancy between the estimated and actual voltages is within a few volts: this deviation is considered acceptable, given the measurement errors added to the EKF-based controller.

In Fig. 4(i) and (j), the power injected into the grid P_g and the output power of the upper arm of phase a $P_{up,a}$ (which is compared with the maximum available one $P_{up,a}^{max}$) using an EKF-based controller are reported. These results can be compared with those in Fig. 4(k) and (l) using the benchmark controller. The two controllers yield very similar performances, especially before and after the step change in irradiance. The transient response to the irradiance changes (at 5 s) varies mostly due to parameter tuning differences in the two controllers.

As to the DMPPT efficiency (i.e., η), the benchmark controller achieves 99.93% and the EKF-based counterpart achieves 99.89% before the disturbance at 5 s. Under the second steady-state condition, the values of η are 99.94% and 99.90% for the benchmark and EKF-based controllers, respectively. This slight difference is illustrated in the three insets of Fig. 4(j) and (l), where it is evident that $P_{\text{up, a}}$ with the benchmark controller is slightly closer to the theoretical value (dashed line) and varies less around its mean. However, it is important to note that the EKF-based controller purposely operates at a lower execution frequency, is influenced by measurement errors, and requires significantly fewer sensors.

Compared with the benchmark controller, the EKF-based controller achieves higher efficiency not only at the steady state, but also during transient operation. This is confirmed by the middle insets of Fig. 4(j) and (l), which show the transient behavior of the system right after the irradiance step change at 5 s using the two controllers. The EKF-based controller exhibits a larger overshoot compared with the benchmark one but reaches the steady-state condition sooner (i.e., 6 s versus 6.5 s). Efficiency is a metric that is typically computed at the steady state: as such, it cannot be quantified just as easily during transient behavior. To provide a metric that conveys a similar meaning under these circumstances, we analyze the difference between $P_{\text{up, a}}^{\max}$ and $P_{\text{up, a}}$ and compute its integral during 5-6.5 s. This integral, which corresponds to an energy loss and is associated with the light blue shaded area in the middle insets, amounts to 21.01 J and 11.33 J for the EKF-based and benchmark controllers, respectively. Once again, this difference may vary depending on a plethora of factors (e. g., regulator parameter tuning), but it is quite small in any case, which confirms the efficiency of EKF-based controller during transient operation.

B. Scenario B: SM Under Non-uniform Irradiance Conditions

In this scenario, the EKF-based controller is tested when the SMs in the upper arm of phase a work under the non-uniform irradiance conditions as shown in Table VI. Simulation results in scenario B are reported in Fig. 5.

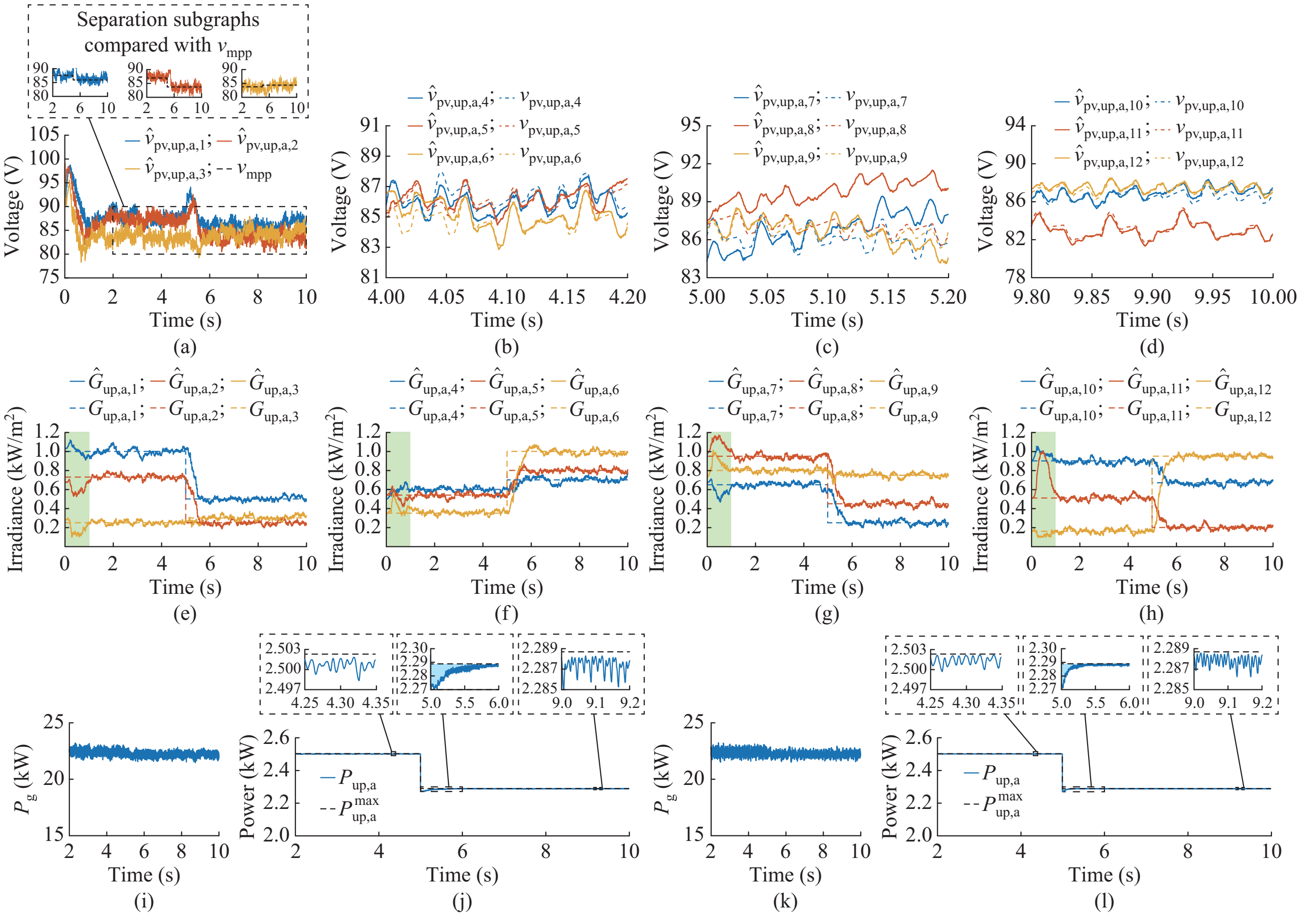

(a) (b) (c) (d)

(e) (f) (g) (h)

(i) (j) (k) (l)

Fig. 5. Simulation results in scenario B. (a) Estimated voltages of SMs 1-3 over entire simulation time. (b) Estimated and actual voltages of SMs 4-6 during 4.0-4.2 s. (c) Estimated and actual voltages of SMs 7-9 during 5.0-5.2 s. (d) Estimated and actual voltages of SMs 10-12 during 9.8-10.0 s. (e) Estimated irradiances of SMs 1-3. (f) Estimated irradiances of SMs 4-6. (g) Estimated irradiances of SMs 7-9. (h) Estimated irradiances of SMs 10-12. (i) P_{g} using EKF-based controller. (j) $P_{\text{up, a}}$ using EKF-based controller. (k) P_{g} using benchmark controller. (l) $P_{\text{up, a}}$ using benchmark controller.

Also, in this scenario, the initial estimates of the SM irradiances and voltages are intentionally set to be different from their true values to highlight the robustness of the EKF-based controller. In the first 5 s, after a short transient, the SM voltages stabilize, on average, at their theoretical optimal values (as shown in Fig. 5(a)) owing to accurate irradiance estimates (as shown in Fig. 5(e)-(h)). Since SMs work at different irradiances, the corresponding operating voltage points differ.

After 5 s, each SM irradiance changes unevenly. Despite the sudden change and non-uniform irradiance distribution, the estimations still stabilize in less than 1 s (as shown in Fig. 5(e)-(h)), and SM voltages settle at the steady state corresponding to their new MPPs (as shown Fig. 5(a)). Also in this scenario, the estimation of SM voltages achieves good results despite noise and measurement errors, as shown in Fig. 5(b)-(d).

As shown in Fig. 5(i) and (k), P_{g} has a higher ripple when the EKF-based controller is adopted. This difference, which is also evident from $P_{\mathrm{up,a}}$ (as shown in Fig. 5(j) and (l)), can be due to the lower execution time and measurement errors introduced in the EKF-based controller.

The middle insets of Fig. 5(j) and (l) compare the transient performance of the EKF-based and benchmark controllers right after the irradiance step changes at 5 s. The former has a larger overshoot and takes longer to reach steady state (i.e., 6 s versus 5.5 s). We compute the energy loss over the time window of 5-6 s, which amounts to 5.36 J and 2.26 J for the EKF-based and benchmark controllers, respectively (i.e., a still very small difference). The effectiveness of the EKF-based controller is also proven under the second steady-state condition, where η is 99.90% (versus 99.94% with the benchmark controller).

C. Effects of Parameter Variations on Key Performance Metrics

Further numerical simulations of scenarios A and B are conducted to evaluate the impact of the execution frequency of EKF-based controller f_{EKF} and the variation of specific PV array parameters, namely $R_{\mathrm{s,ref}}$ and $R_{\mathrm{sh,ref}}$, on key performance metrics. The following performance metrics are defined and analyzed: ① the DMPPT efficiency η of the EKF-based controller at the steady state, ② the average mean absolute percentage error (MAPEs) of the estimated voltages $\overline{MAPE_v}$ and irradiances $\overline{MAPE_G}$, and ③ the maximum convergence time of the irradiance estimation $t_{\mathrm{conv},G}^{\max}$ to the steady state. Given that the SM voltages are continuous variables, the average MAPE between the estimated and actual values is calculated over the entire simulated time range. On the contrary, since the true irradiance exhibits discontinuities at 5 s, their average MAPE is assessed before and after that time, as soon as the estimates converge to the steady state.

The parameter variations and related performance metrics are listed in Tables VII and VIII, corresponding to scenarios A and B, respectively.

TABLE VII
PARAMETER VARIATIONS AND RELATED PERFORMANCE METRICS IN SCENARIO A

f_{EKF} (kHz)	Changing condition of $R_{\mathrm{s,ref}}$ and $R_{\mathrm{sh,ref}}$	$\overline{MAPE_v}$ (%)	Before irradiance changes			After irradiance changes		
			η (%)	$\overline{MAPE_G}$ (%)	$t_{\mathrm{conv},G}^{\max}$ (s)	η (%)	$\overline{MAPE_G}$ (%)	$t_{\mathrm{conv},G}^{\max}$ (s)
6	Base case	0.88	99.89	1.82	1.27	99.90	4.58	0.90
3	Base case	1.07	99.89	3.98	1.18	99.90	8.97	0.90
1	Base case	1.65	99.89	4.28	1.68	99.90	9.56	1.13
6	$R_{\mathrm{s,ref}}$ and $R_{\mathrm{sh,ref}}$ are changed for all SMs with a 10% standard deviation	0.88	99.88	1.92	1.22	99.89	4.42	0.86
6	$R_{\mathrm{s,ref}}$ is doubled for all SMs	0.92	99.00	4.28	1.36	99.07	4.71	0.84
6	$R_{\mathrm{s,ref}}$ is tripled for all SMs	0.91	96.40	9.47	1.32	96.67	5.55	0.81

TABLE VIII
PARAMETER VARIATIONS AND RELATED PERFORMANCE METRICS IN SCENARIO B

f_{EKF} (kHz)	Changing condition of $R_{\mathrm{s,ref}}$ and $R_{\mathrm{sh,ref}}$	$\overline{MAPE_v}$ (%)	Before irradiance changes			After irradiance changes		
			η (%)	$\overline{MAPE_G}$ (%)	$t_{\mathrm{conv},G}^{\max}$ (s)	η (%)	$\overline{MAPE_G}$ (%)	$t_{\mathrm{conv},G}^{\max}$ (s)
6	Base case	1.03	99.90	4.05	1.40	99.90	4.13	1.05
3	Base case	1.31	99.90	6.81	1.72	99.90	7.67	1.24
1	Base case	2.28	99.90	8.94	2.02	99.90	9.46	1.98
6	$R_{\mathrm{s,ref}}$ and $R_{\mathrm{sh,ref}}$ are changed for all SMs with a 10% standard deviation	0.99	99.89	3.95	1.39	99.89	3.76	1.03
6	$R_{\mathrm{s,ref}}$ is doubled for all SMs	1.08	99.04	5.09	1.39	99.05	4.87	1.07
6	$R_{\mathrm{s,ref}}$ is tripled for all SMs	0.95	96.57	7.06	1.38	96.61	7.15	1.06

We test how the MMC-based PV system performs using EKF-based controller when f_{EKF}, $R_{\mathrm{s,ref}}$, and $R_{\mathrm{sh,ref}}$ change for two reasons.

1) Firstly, one may argue that, compared with an MMC-based PV system based on benchmark controller, the one based on EKF has a higher computational burden, as the EKF block in Fig. 2(b) has to run continuously, thus requiring more powerful hardware. This is true to an extent, as the additional computational burden may be limited by reducing f_{EKF}. By so doing, the EKF block would be executed less frequently. This can be done as long as changes in f_{EKF} do not compromise the MMC operation.

2) Secondly, the EKF-based controller needs a model (i.e., the expressions of $\boldsymbol{f}$ and $\boldsymbol{h}$ in (11) and (13)) that closely matches the behavior of the controlled system to properly work. However, one must verify that the EKF-based controller adequately handles discrepancies in model parameters that inevitably arise due to an imperfect knowledge of the real system. For example, $R_{\mathrm{s,ref}}$ and $R_{\mathrm{sh,ref}}$ may differ in each PV array by construction or due to aging.

To evaluate the impact of f_{EKF}, three values of which are chosen for analysis: 6, 3, and 1 kHz. In the simulations corresponding to the first three rows of Tables VII and VIII, no further variations in the converter model parameters are assumed. Reducing f_{EKF} from 6 to 1 kHz does not decrease the DMPPT efficiency. Small estimation errors, particularly in irradiance, do not impact the MPP voltage of PV array and, thus, efficiency. In scenario B, the maximum convergence time nearly doubles at lower frequencies. Aside from this, the steady-state conditions are achieved in a few seconds, with high DMPPT efficiency and accurate voltage and irradiance estimates (i.e., $\overline{MAPE}_v$ and $\overline{MAPE}_G$ are lower than 10%).

Among the tested cases, that with $f_{\mathrm{EKF}}=1$ kHz exhibits the poorest performance across all metrics except for the DMPPT efficiency, which remains identical across all cases. This is particularly evident in Fig. 6, which presents the estimated voltage of SM 1 and the estimated irradiance of SMs 1-3 in scenario B at different f_{EKF} values, which are compared with their true values. In each case, the highest estimation errors occur right after the irradiance shift at 5 s. By reducing f_{EKF}, higher errors are incurred for longer durations after 5 s primarily due to longer convergence time witnessed at lower frequencies. However, the steady-state performance remains satisfactory across all frequencies, with high-frequency oscillations in the estimates being reduced at lower f_{EKF}. On the one hand, increasing f_{EKF} improves the precision and shortens the convergence time under the transient conditions. On the other hand, higher frequencies introduce substantial implementation challenges, especially for micro-controllers, as they demand increased computational resources. Thus, the tuning of f_{EKF} must stem from a trade-off between accuracy required and processing capacity available.

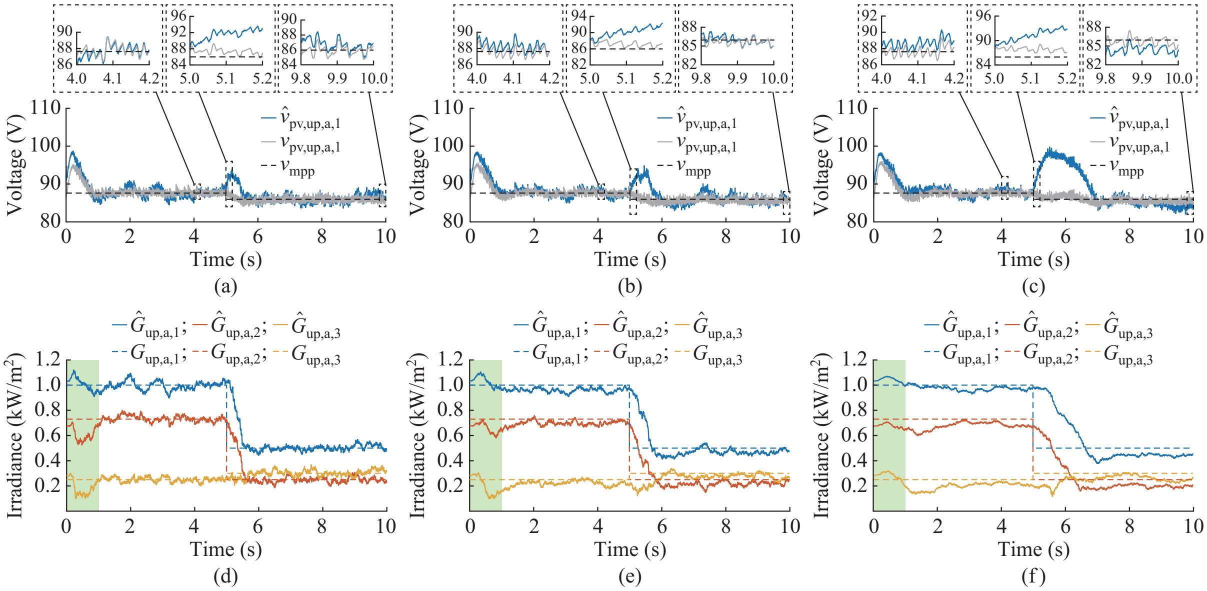

(a) (b) (c)

(d) (e) (f)

Fig. 6. Impact of f_{EKF} in scenario B. (a) Estimated and true voltages of SM 1 at $f_{\mathrm{EKF}}=6$ kHz. (b) Estimated and true voltages of SM 1 at $f_{\mathrm{EKF}}=3$ kHz. (c) Estimated and true voltages of SM 1 at $f_{\mathrm{EKF}}=1$ kHz. (d) Estimated and true irradiances of SMs 1-3 at $f_{\mathrm{EKF}}=6$ kHz. (e) Estimated and true irradiances of SMs 1-3 at $f_{\mathrm{EKF}}=3$ kHz. (f) Estimated and true irradiances of SMs 1-3 at $f_{\mathrm{EKF}}=1$ kHz.

To evaluate the impact of changes in PV array parameters, we vary $R_{\mathrm{s,ref}}$ and $R_{\mathrm{sh,ref}}$ in three ways, as shown in Tables VII and VIII. To reflect differences in PV array characteristics due to manufacturing variations, we change $R_{\mathrm{s,ref}}$ and $R_{\mathrm{sh,ref}}$ with a 10% standard deviation. We also consider aging effects or temperature-induced changes by doubling and tripling $R_{\mathrm{s,ref}}$ for all SMs [42]. While doing so, f_{EKF} is fixed at 6 kHz. The results in the last three rows of Tables VII and VIII indicate that these parameter variations primarily affect the DMPPT efficiency and irradiance estimation, while the SM voltage estimation and the maximum convergence time of irradiance estimation remain largely unaffected and practically unchanged compared with the base case. This behavior can be attributed to the strong dependence of irradiance estimation on accurate PV array parametrization. Significant deviations in irradiance estimation lead to a sub-optimal reference MPP voltage, ultimately reducing the DMPPT efficiency of the EKF-based controller. Despite this, even when tripling $R_{\mathrm{s,ref}}$, the DMPPT efficiency remains satisfactory, with about a 3% efficiency loss compared with the base case. In scenarios where the DMPPT efficiency might become low (e.g., due to PV array aging), re-characterizing the PV array model would effectively restore the system performance.

V. CONCLUSION

In this paper, a control strategy for a three-phase MMC-based PV system is proposed. The EKF-based controller grants a highly efficient DMPPT and requires less sensors than similar-purpose MMC based on P&O methods, yet achieving comparable performances. In particular, the number of sensors required is always the same regardless of the number of PV arrays installed in each MMC arm.

Simulation results show that the EKF-based controller provides accurate estimates (i.e., up to 10% MAPE) of individual SM voltages and irradiances. These outputs, together with the characteristic of PV arrays, can be employed to determine the optimal reference voltage for each SM, which are used by the MMC controllers to regulate the system.

Estimation accuracy is proven both under uniform and non-uniform irradiance conditions by adding measurement noises and significantly deviating some PV array parameters (i. e., $R_{\mathrm{s,ref}}$ and $R_{\mathrm{sh,ref}}$) from those used in the EKF due to manufacturing variations, aging effects, or temperature-induced changes. Estimation accuracy is also ensured when f_{EKF} is reduced from 6 to 1 kHz to limit the computational burden of the EKF-based controller. Moreover, after sudden changes in irradiance, their estimates converge in less than 2 s, thus proving that the EKF-based controller can quickly react to shading phenomena.

Overall, the EKF-based controller is a valid solution for PV integration at the SM level through MMC, as it circumvents the need for a multitude of sensors required in analogous applications. Using estimation techniques, such as the EKF, to reduce the number of sensors can contribute to the adoption of MMC as a means to integrate different energy sources (not necessarily PV systems) at the SM level, i.e., a solution that is recently gaining momentum in the literature.

Future work is aimed at extending the EKF-based controller to estimating the temperature of PV arrays (here assumed to be known) and detect changes in their parameters due to aging or temperature-induced effects.

REFERENCES

[1] M. Kasper, D. Bortis, and J. W. Kolar, “Classification and comparative evaluation of PV panel-integrated DC-DC converter concepts,” *IEEE Transactions on Power Electronics*, vol. 29, no. 5, pp. 2511-2526, May 2014.

[2] L. Bowtell and A. Ahfock, “Direct current offset controller for transformerless single-phase photovoltaic grid-connected inverters,” *IET Renewable Power Generation*, vol. 4, no. 5, pp. 428-437, Sept. 2010.

[3] L. Wu, Z. Zhao, and J. Liu, “A single-stage three-phase grid-connected photovoltaic system with modified MPPT method and reactive power compensation,” *IEEE Transactions on Energy Conversion*, vol. 22, no. 4, pp. 881-886, Dec. 2007.

[4] K. Chen, S. Tian, Y. Cheng *et al*., “An improved MPPT controller for photovoltaic system under partial shading condition,” *IEEE Transactions on Sustainable Energy*, vol. 5, no. 3, pp. 978-985, Jul. 2014.

[5] I. R. Balasubramanian, S. I. Ganesan, and N. Chilakapati, “Impact of partial shading on the output power of PV systems under partial shading conditions,” *IET Power Electronics*, vol. 7, no. 3, pp. 657-666, Mar. 2014.

[6] A. Bidram, A. Davoudi, and R. S. Balog, “Control and circuit techniques to mitigate partial shading effects in photovoltaic arrays,” *IEEE Journal of Photovoltaics*, vol. 2, no. 4, pp. 532-546, Oct. 2012.

[7] J. W. Zapata, S. Kouro, G. Carrasco *et al*., “Analysis of partial power DC-DC converters for two-stage photovoltaic systems,” *IEEE Journal of Emerging and Selected Topics in Power Electronics*, vol. 7, no. 1, pp. 591-603, May 2018.

[8] H. Keyhani and H. A. Toliyat, “Single-stage multistring PV inverter with an isolated high-frequency link and soft-switching operation,” *IEEE Transactions on Power Electronics*, vol. 29, no. 8, pp. 3919-3929, Aug. 2014.

[9] I. Abdalla, J. Corda, and L. Zhang, “Multilevel DC-link inverter and control algorithm to overcome the PV partial shading,” *IEEE Transactions on Power Electronics*, vol. 28, no. 1, pp. 14-18, Jan. 2013.

[10] Y. Hu, J. Wu, W. Cao *et al*., “Ultrahigh step-up DC-DC converter for distributed generation by three degrees of freedom (3DoF) approach,” *IEEE Transactions on Power Electronics*, vol. 31, no. 7, pp. 4930-4941, Jul. 2016.

[11] S. M. Bose, M. O. Badawy, and Y. Sozer, “A novel differential power processing architecture for a partially shaded PV string using distributed control,” in *Proceedings of 2018 IEEE Energy Conversion Congress and Exposition*, Portland, USA, Sept. 2018, pp. 6220-6227.

[12] S. R. Pendem, S. Mikkili, and P. K. Bonthagorla, “PV distributed-MPP tracking: total-cross-tied configuration of string-integrated-converters to extract the maximum power under various PSCs,” *IEEE Systems Journal*, vol. 14, no. 1, pp. 1046-1057, Jun. 2019.

[13] R. López-Erauskin, A. González, G. Petrone *et al*., “Multi-variable perturb and observe algorithm for grid-tied PV systems with joint central and distributed MPPT configuration,” *IEEE Transactions on Sustainable Energy*, vol. 12, no. 1, pp. 360-367, Jan. 2021.

[14] B. Xiao, L. Hang, J. Mei *et al*., “Modular cascaded H-bridge multilevel PV inverter with distributed MPPT for grid-connected applications,” *IEEE Transactions on Industry Applications*, vol. 51, no. 2, pp. 1722-1731, Mar. 2015.

[15] D. Iannuzzi, L. Piegari, and P. Tricoli, “A novel PV-modular multilevel converter for building integrated photovoltaics,” in *Proceedings of 2013 Eighth International Conference and Exhibition on Ecological Vehicles and Renewable Energies*, Monte Carlo, Monaco, Mar. 2013, pp. 1-7.

[16] Y. Yu, G. Konstantinou, B. Hredzak *et al*., “Power balance optimization of cascaded H-bridge multilevel converters for large-scale photovoltaic integration,” *IEEE Transactions on Power Electronics*, vol. 31, no. 2, pp. 1108-1120, Feb. 2015.

[17] Y. Yu, G. Konstantinou, C. D. Townsend *et al*., “Comparison of zero-sequence injection methods in cascaded H-bridge multilevel converters for large-scale photovoltaic integration,” *IET Renewable Power Generation*, vol. 11, no. 5, pp. 603-613, Apr. 2017.

[18] J. Echeverría, S. Kouro, M. Pérez *et al*., “Multi-modular cascaded DC-DC converter for HVDC grid connection of large-scale photovoltaic power systems,” in *Proceedings of IECON 2013-39th Annual Conference of the IEEE Industrial Electronics Society*, Vienna, Austria, Nov. 2013, pp. 6999-7005.

[19] S. Rivera, B. Wu, R. Lizana *et al*., “Modular multilevel converter for large-scale multistring photovoltaic energy conversion system,” in *Proceedings of 2013 IEEE Energy Conversion Congress and Exposition*, Denver, USA, Sept. 2013, pp. 1941-1946.

[20] F. Rong, X. Gong, and S. Huang, “A novel grid-connected PV system based on MMC to get the maximum power under partial shading conditions,” *IEEE Transactions on Power Electronics*, vol. 32, no. 6, pp. 4320-4333, Jun. 2017.

[21] H. Bayat and A. Yazdani, “A power mismatch elimination strategy for an MMC-based photovoltaic system,” *IEEE Transactions on Energy Conversion*, vol. 33, no. 3, pp. 1519-1528, Sept. 2018.

[22] S. Barcellona, M. Barresi, S. Colnago *et al*., “MMC-PV system with DC-link integrated battery energy storage system,” in *Proceedings of 2021 IEEE 15th International Conference on Compatibility, Power Electronics and Power Engineering*, Florence, Italy, Jul. 2021, pp. 1-8.

[23] S. Barcellona, M. Barresi, and L. Piegari, “MMC-based PV three-phase system with distributed MPPT,” *IEEE Transactions on Energy Conversion*, vol. 37, no. 3, pp. 1567-1578, Apr. 2022.

[24] A. Lesnicar and R. Marquardt, “An innovative modular multilevel converter topology suitable for a wide power range,” in *Proceedings of 2003 IEEE Bologna Power Tech Conference Proceedings*, Bologna, Italy, Jun. 2004, pp. 1-6.

[25] D. del Giudice, F. Bizzarri, D. Linaro *et al*., *Modular Multilevel Converter Modelling and Simulation for HVDC Systems: State of the Art and a Novel Approach*. New York: Springer Nature, 2022.

[26] M. A. Perez, S. Ceballos, G. Konstantinou *et al*., “Modular multilevel converters: recent achievements and challenges,” *IEEE Open Journal of the Industrial Electronics Society*, vol. 2, pp. 224-239, Feb. 2021.

[27] T. Soong and P. W. Lehn, “Evaluation of emerging modular multilevel converters for BESS applications,” *IEEE Transactions on Power Delivery*, vol. 29, no. 5, pp. 2086-2094, Oct. 2014.

[28] A. I. Elsanabary, G. Konstantinou, S. Mekhilef *et al*., “Medium voltage large-scale grid-connected photovoltaic systems using cascaded H-bridge and modular multilevel converters: a review,” *IEEE Access*, vol. 8, pp. 223686-223699, Dec. 2020.

[29] M. Barresi, D. de Simone, and L. Piegari, “Optimization of MMC level number for battery integration in MV grid,” in *Proceedings of 2020*

International Symposium on Power Electronics, *Electrical Drives*, *Automation and Motion*, Sorrento, Italy, pp. 744-750, Jun. 2020.
[30] S. Barcellona, M. Barresi, and L. Piegari, "MMC-based PV single-phase system with distributed MPPT," *Energies*, vol. 13, no. 15, p. 3964, Aug. 2020.
[31] A. Ghazanfari and Y. A. I. Mohamed, "A hierarchical permutation cyclic coding strategy for sensorless capacitor voltage balancing in modular multilevel converters," *IEEE Journal of Emerging and Selected Topics in Power Electronics*, vol. 4, no. 2, pp. 576-588, Jul. 2015.
[32] F. Deng, C. Liu, Q. Wang *et al*., "A currentless submodule individual voltage balancing control for modular multilevel converters," *IEEE Transactions on Industrial Electronics*, vol. 67, no. 11, pp. 9370-9382, Nov. 2020.
[33] R. He, D. Liu, R. Teodorescu *et al*., "An improved submodule capacitor voltage measuring algorithm for MMC with reduced sensors," *IEEE Sensors Journal*, vol. 21, no. 18, pp. 20475-20492, Sept. 2021.
[34] G. Pizarro, P. Poblete, G. Droguett *et al*., "Extended Kalman filtering for full-state estimation and sensor reduction in modular multilevel converters," *IEEE Transactions on Industrial Electronics*, vol. 70, no. 2, pp. 1927-1938, Feb. 2023.
[35] L. Testa, O. Kalmbach, and C. M. Hackl, "A generic Lyapunov-based observer for double-star-chopper-cell/bridge-cell modular-multilevel-cascade-converters," in *Proceedings of 2023 IEEE 32nd International Symposium on Industrial Electronics*, Helsinki, Finland, Jun. 2023, pp. 1-6.
[36] E. Kabalci and A. Boyar, "Highly efficient interleaved solar converter controlled with extended Kalman filter MPPT," *Energies*, vol. 15, no. 21, p. 7838, Nov. 2022.
[37] D. J. Docimo, M. Ghanaatpishe, and A. Mamun, "Extended Kalman filtering to estimate temperature and irradiation for maximum power point tracking of a photovoltaic module," *Energy*, vol. 120, pp. 47-57, Feb. 2017.
[38] W. Tian, P. Shen, G. M. de Sousa *et al*., "Voltage sensor reduction method for modular multilevel converters based on a simple voltage reconstruction approach," in *Proceedings of 2023 IEEE 8th Southern Power Electronics Conference and 17th Brazilian Power Electronics Conference*, Florianopolis, Brazil, Nov. 2023, pp. 1-7.
[39] H. Akagi, "Classification, terminology, and application of the modular multilevel cascade converter (MMCC)," *IEEE Transactions on Power Electronics*, vol. 26, no. 11, pp. 3119-3130, Nov. 2011.
[40] G. Bishop and G. Welch, "An introduction to the Kalman filter," *Proceedings of SIGGRAPH, Course*, vol. 8, p. 41, May 2001.
[41] M. L. Orozco-Gutierrez, G. Spagnuolo, C. A. Ramos-Paja *et al*., "Enhanced simulation of total cross tied photovoltaic arrays," *Mathematics and Computers in Simulation*, vol. 158, pp. 49-64, Apr. 2019.
[42] J. D. Bastidas-Rodríguez, E. Franco, G. Petrone *et al*., "Model-based degradation analysis of photovoltaic modules through series resistance estimation," *IEEE Transactions on Industrial Electronics*, vol. 62, no. 11, pp. 7256-7265, Nov. 2015.

Marzio Barresi received the M.S. and Ph.D. degrees in electrical engineering from Polytechnic University of Milan, Milan, Italy, in 2019 and 2023, respectively. Since 2023, he has been with the Department of Electronics, Information, and Bioengineering at Polytechnic University of Milan, where he currently serves as a Researcher in the Electric Power Systems and Power Electronics Research Group. His research interests include renewable generation system, electric vehicle, energy storage system, control and modeling of modular multilevel converter, and power electronics-dominated power system.

Davide del Giudice received the M.S. and Ph.D. degrees in electrical engineering from Polytechnic University of Milan, Milan, Italy, in 2017 and 2022, respectively. He is currently a Researcher with the Department of Electronics, Information and Bioengineering, Polytechnic University of Milan. His research interests include simulation techniques for electric power system with a high penetration of converter-interfaced elements, such as high-voltage direct current system, electric vehicle, and generation fuelled by renewables.

Davide de Simone obtained the master's and Ph.D. degrees in electrical engineering from Polytechnic University of Milan, Milan, Italy, in 2017 and 2021, respectively. He is currently a Researcher at the Department of Electronics, Information, and Bioengineering (DEIB) at Polytechnic University of Milan, working in the Electric Power Systems and Power Electronics Research Group. His research interests include modular multilevel converter, open-ended electrical drive, and energy storage system.

Samuele Grillo received the Laurea degree in electronic engineering and the Ph.D. degree in power system from the University of Genova, Genova, Italy, in 2004 and 2008, respectively. He is currently an Associate Professor with the Dipartimento di Elettronica, Informazione e Bioingegneria, Polytechnic University of Milan, Milan, Italy. Since 2018, he has been a Contributor to CIGRÉ Working Group B5.65 "Enhancing Protection System Performance by Optimising the Response of Inverter-Based Sources". His research interests include smart grid, integration of distributed renewable source, energy storage device in power network, and optimization and control techniques applied to power system.